

# A 10 mm<sup>3</sup> Inductive Coupling Radio for Syringe-Implantable Smart Sensor Nodes

Yao Shi, *Student Member, IEEE*, Myungjoon Choi, *Student Member, IEEE*, Ziyun Li, *Student Member, IEEE*, Zhihong Luo, Gyouho Kim, *Member, IEEE*, Zhiyoong Foo, Hun-Seok Kim, *Member, IEEE*, David D. Wentzloff, *Member, IEEE*, and David Blaauw, *Fellow, IEEE*

**Abstract**—We present a near-field radio system for a millimeter-scale wireless smart sensor node that is implantable through a 14-gauge syringe needle. The proposed system integrates a radio system on chip and a magnetic antenna on a glass substrate within a total dimension of  $1 \times 1 \times 10$  mm<sup>3</sup>. We demonstrate energy-efficient active near-field wireless communication between the millimeter-scale sensor node and a base station device through an RF energy-absorbing tissue. The wireless transceiver, digital baseband controller, wakeup controller, on-chip baseband timer, sleep timer, and MBUS controller are all integrated on the SoC to form a millimeter-scale sensor node, together with a  $1 \times 8$  mm<sup>2</sup> magnetic antenna fabricated with a 1.5- $\mu$ m-thickness gold on a 100  $\mu$ m-thickness glass substrate. An asymmetric link is established pairing the sensor antenna with a codesigned  $11 \times 11$  cm<sup>2</sup> base station antenna to achieve a link distance of up to 50 cm for sensor transmission and 20 cm for sensor reception. The transmitter consumes a 43.5  $\mu$ W average power at 2 kb/s, while the receiver power consumption is 36  $\mu$ W with a  $-54$  dBm sensitivity at 100 kb/s. When powered by a  $1 \times 2.2$  mm<sup>2</sup> thin-film battery (2  $\mu$ Ah, 4.1 V), the designed system has a two week expected lifetime without battery recharging when the system wakes up and transmits and receives 16 b data every 10 min.

**Index Terms**—Asymmetric inductive link, low power, millimeter scale, syringe implantable, system on chip (SoC).

## I. INTRODUCTION

IMPLANTABLE smart devices are gaining attention due to their potential uses in medical and healthcare applications that aim to improve the quality of human life. Beyond well-known applications such as pacemakers [1] and cochlear implants [2], we envision millimeter-scale smart implantable devices that can perform long-term sensing, local computation, real-time actuation, and data transfer.

As shown in Fig. 1, there has been a continuous trend to shrink the volume of implantable pacemakers [3]. While their volume has been reduced dramatically, their minimum

Manuscript received April 9, 2016; revised July 6, 2016; accepted August 23, 2016. Date of publication September 28, 2016; date of current version October 29, 2016. This paper was approved by Guest Editor Wentai Liu. This work was supported by the National Science Foundation under Grant CNS-1111541.

Y. Shi is with the Department of Electrical and Computer Engineering, University of Michigan, Ann Arbor, MI 48105 USA (e-mail: yaoshi@umich.edu).

M. Choi, Z. Li, Z. Luo, G. Kim, Z. Foo, H.-S. Kim, D. D. Wentzloff, and D. Blaauw are with the University of Michigan, Ann Arbor, MI 48105 USA.

Color versions of one or more of the figures in this paper are available online at <http://ieeexplore.ieee.org>.

Digital Object Identifier 10.1109/JSSC.2016.2606162

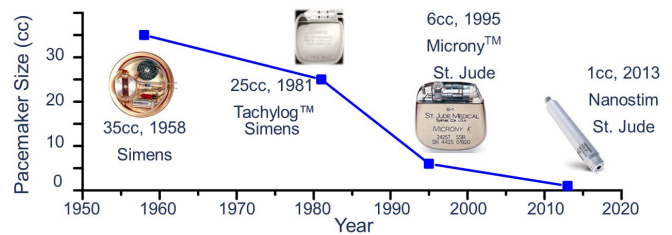


Fig. 1. Long-term trend of implantable pacemaker size over years [3].

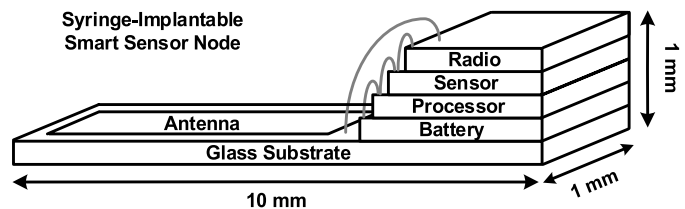


Fig. 2. Targeted syringe-implantable smart sensor node with proposed radio and other functional layers.

size still remains around 1 cm<sup>3</sup>, a size that requires invasive and more risky surgery for implantation. Meanwhile, passive RF tags are available with a much smaller volume—approximately 12 mm<sup>3</sup> (a 83 $\times$  volume reduction) [4]. These small devices can be implanted through a syringe needle, minimally affecting a patient's everyday life. However, these implantable radio-frequency identification (RFID) tags are passive devices that are only powered when a reader is in proximity. This lack of an integrated power source makes RFID devices incapable of performing the complicated duties that we envision for implantable smart devices. In addition, injectable microstimulators have been presented with active functions including neuromuscular stimulation and data communication [5]–[7]. However, to support complicated active operations, those implants typically incorporate a large chip, many off-chip components, and a bulky battery, hindering further miniaturization.

The goal of this paper is to enable the development of implantable smart devices that are much smaller than 1 cm<sup>3</sup> but still have the ability to perform autonomous medical functions with a restricted local power source. This idea has driven the proposed syringe-implantable smart sensor node, whose conceptual configuration is shown in Fig. 2. The system is constructed from several layers (chips) that are stacked and

connected through wire bonding [8]. The thickness of each layer is approximately 100  $\mu\text{m}$ . All layers, including the radio, a processor, a thin-film battery, and other peripherals, such as sensor layer and power management layer, are implemented with fully integrated circuits eliminating external off-chip components, which allows reduction in size. Furthermore, compared with placing all circuits in single large chip [5], [6], the stack-based integration scheme reduces overall system volume and enables increased system functionality [8]. The sensor node's overall  $1 \times 1 \times 10 \text{ mm}^3$  form factor is specifically tailored to make it implantable through a 14-gauge syringe needle, eliminating the need for surgery. There has been continual research to realize a millimeter-scale ultralow power (ULP) sensor system with multiple functional layers powered by a thin-film battery [9], [10]. This paper introduces a new solution to enable long distance ( $>20 \text{ cm}$ ) near-field communication between these millimeter-scale ULP wireless sensor nodes and a base station through tissue.

There are many unique challenges for a radio system that is constrained to a millimeter-scale syringe-implantable form factor. To fit into a syringe needle, the antenna dimension is strictly constrained to a millimeter or less in width. Because this dimension is much smaller than the wavelength (e.g., 3 m for 100 MHz), the antenna gain is very poor. In addition, the RF wireless communication link distance is significantly constrained by the severe signal loss in an electromagnetic field-absorbing tissue. A third major challenge is the extreme energy and power constraints imposed on the system. A thin-film battery limited in size to  $1 \times 2.2 \text{ mm}^2$  provides only 2  $\mu\text{Ah}$ . Moreover, its peak power is less than 50  $\mu\text{W}$  due to the high intrinsic resistance [11]. These limitations present a challenge in designing radio transceiver circuits, which typically consume  $>100 \mu\text{W}$  active power. Addressing these challenges is the topic of this paper.

A number of works have been presented on ultrasmall implanted radios. Backscattering, in which the passive radio in a sensor node reflects an incoming signal from a base station or a reader, is the most common method used to realize ULP consumption [12], [13]. These works consume approximately 1  $\mu\text{W}$  with a small system volume, on the order of several cubic millimeters. However, backscattering suffers from reader self-jamming, limiting the communication range to less than 3.5 cm [13], [14]. Wirelessly powered sensor nodes that achieve longer communication distances exist (see [14]), but they typically require bulky off-chip passive components that do not fit in the millimeter-scale form factor. In contrast, active radios can support significantly longer ranges [15], [16] with a smaller volume. In [15], a 1.5 mm<sup>3</sup> complete system with an active transmitter was reported. However, this design includes only a transmitter, and its active power consumption is rather high (45 mW). An active transceiver with an on-off keying (OOK) transmitter and a super-regenerative receiver is proposed in [16] to obtain a range greater than 10 cm. However, the system is codesigned with a 2.3 cm  $\times$  2.4 cm loop antenna that is unacceptable for a millimeter-scale system.

We propose three techniques by which to realize a ULP millimeter-scale implanted sensor node communication system.



Fig. 3. Proposed millimeter-scale radio system within a syringe needle on top of a one cent coin. Note that further die stacking and hermetic encapsulation are necessary for final implantation.

- 1) A codesigned asymmetric magnetic antenna pair on the implanted sensor node and the base station device.
- 2) A pulse-inject H-bridge oscillator with improved efficiency that replaces a conventional constant-bias cross-coupled oscillator [15], [16].
- 3) A new *sensor-initiated* synchronization protocol in which timing offset estimation is performed on the base station, eliminating the need for an area-demanding off-chip crystal and synchronization baseband processing on the sensor node and thereby significantly improving its energy efficiency.

Combining these techniques, the proposed system achieves a link distance up to 50 cm for sensor transmission (TX) and 20 cm for sensor reception (RX) through 3 cm of tissue. The system fully integrates the transceiver, baseband controller, timer, wakeup controller, and MBUS controller [17] on a single chip together with a millimeter-scale magnetic antenna fabricated on a glass substrate [18].

This paper is organized as follows. Section II describes the sensor-initiated communication and the wakeup and sleep control circuits. Section III describes the design and analysis of the antenna. Section IV describes the circuit design of the transceiver. Section V presents measurement results using the proposed system, and Section VI then concludes this paper.

## II. OVERVIEW OF SYSTEM

### A. System Overview

Fig. 3 is a photo of the proposed radio system that fits into a 14-gauge syringe needle. The syringe implantation constrains the width of the system to approximately 1 mm, whereas the length can be significantly more than 1 mm. Note that it is the antenna, rather than the radio chip, that dominates the overall system volume. The sensor node's magnetic antenna is  $1 \times 8 \text{ mm}^2$  in size and is printed on top of the 100- $\mu\text{m}$ -thick glass substrate. The radio chip is designed to be 1 mm wide to fully utilize the available area yet fit into the syringe. The chip sits on the same glass substrate and is connected to the antenna by wire bonding. It is worth mentioning that Fig. 3 shows a proposed radio, which is the focus of this paper,

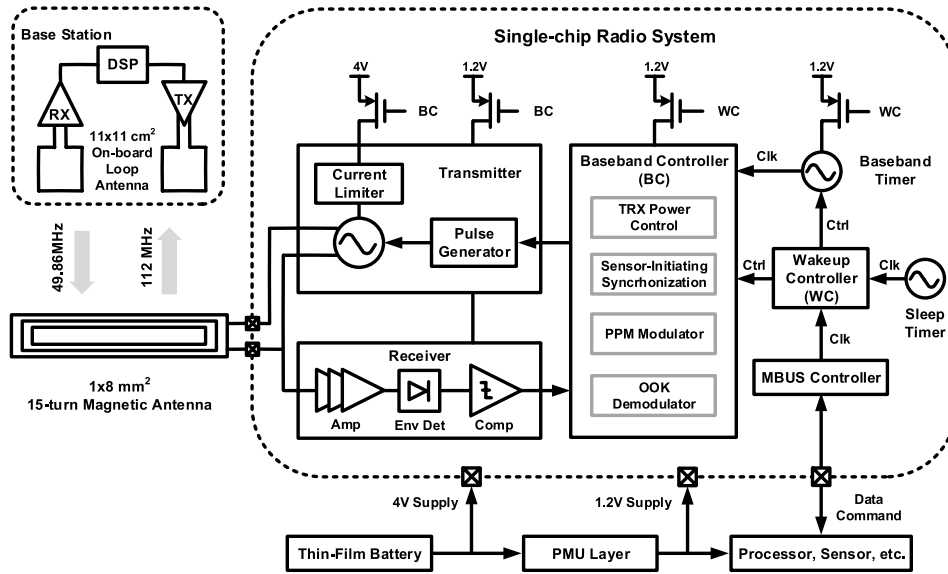


Fig. 4. Proposed single-chip radio system with a  $1 \times 8 \text{ mm}^2$  glass substrate antenna for wireless communication between the sensor node and the base station.

rather than the target sensor node. A complete system requires the integration with other functional layers (processor, thin-film battery, power management unit, and other peripherals) by die stacking and wire bonding [7], which will increase the size of the system by approximately 0.5 mm in height (width and length would remain essentially the same). Moreover, hermetic encapsulation (e.g., glass capsule) of the overall system is necessary for the final implantation [5], [6] and would add approximately 400  $\mu\text{m}$  to each dimension. If so, a final packaged sensor node is expected to fit into a 13-gauge needle, which has an inner diameter of 1.8 mm.

Fig. 4 shows the system block diagram. The proposed radio for the sensor node exchanges data with the base station through near-field inductive coupling, which is a common method for through-tissue communication. It is worth noting that the antennas on the millimeter-scale sensor node and the base station have dissimilar dimensions that are codesigned to enhance coupling strength. The antenna dimension in the sensor node is  $1 \times 8 \text{ mm}^2$ , whereas the base station antenna size is  $11 \times 11 \text{ cm}^2$ . The bidirectional link between the sensor node and the base station utilizes asymmetric carrier frequencies: 112 MHz for sensor node TX (i.e., uplink) and 49.86 MHz for sensor node RX (i.e., downlink). Justification for this asymmetric link design will be discussed in Section III. In the SoC, the power oscillator in the pulsed transmitter operates directly from the battery (4.1 V), whereas other blocks, including transmitter (except power oscillator), receiver, baseband controller, on-chip timer, wakeup controller, and sleep timer, operate on 1.2 V supply. Since this radio SoC is designed to be integrated with other functional layers (e.g., the processor and sensor), a power management unit [19] on one of the system layers generates the global 1.2 V supply, which is downconverted from a battery supply. In the target ULP sensor node with a stack of multiple layers, the designed radio can exchange data and command with other layers via an MBUS interface [17].

### B. Sensor-Initiated Synchronization

Timing synchronization is a critical part of the wireless sensor communication. In general, timing synchronization is performed at the receiver using digital baseband signal processing to estimate and compensate for the symbol timing and baseband sampling frequency offsets. The timing synchronization complexity depends on the mismatch between the transmitter and the receiver baseband clocks. Conventionally, an accurate baseband clock is realized using a phase-locked loop with an accurate frequency reference. A typical frequency reference is a quartz crystal, which is not feasible for millimeter-scale sensor nodes due to its large volume [20]. Alternatively, an on-chip timer can be used to reduce the system volume [21]. However, its frequency accuracy is significantly worse than that of a crystal oscillator, which means the baseband must search for a wider frequency offset, causing high power consumption in the digital baseband circuits [22]. In conventional wireless sensor nodes, a low-power wakeup receiver is always powered on and listens for the initiation packet [23]. However, if a low-accuracy on-chip timer is used, system power is dominated by baseband circuits, making it impractical to realize communication with a wakeup receiver in millimeter-scale sensor nodes.

As shown in Fig. 5, we propose a new energy-efficient *sensor-initiated* synchronization scheme. Since the base station can be much larger than the sensor node, it has a much less constrained power budget. In some cases, the base station can even be powered directly from the electrical grid. At the cost of power consumption and system volume, the base station has excellent receiver sensitivity and digital processing ability. Therefore, in the idle state, the sensor node is sleeping in order to save energy, while the base station receiver is always listening because of its relaxed power budget. Periodically, the sensor node initiates communication by transmitting a packet starting with multiple pulses at a predefined pseudo-random interval (i.e., a header). Once the base station detects

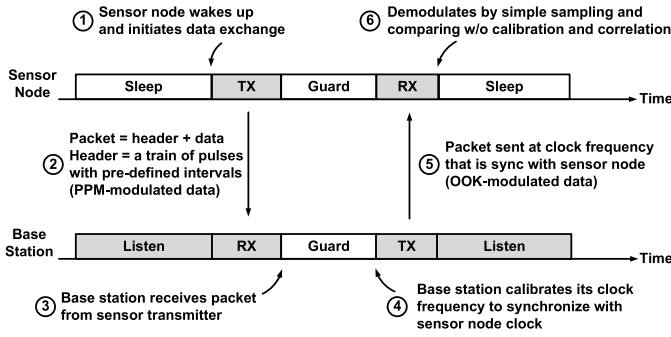


Fig. 5. Conceptual explanation of proposed sensor-initiated synchronization.

the packet, it accurately estimates the baseband timing offset of the sensor node, adjusts its local timer frequency accordingly, and then sends a response packet after a precise (using the timing offset correction) predefined guard time delay set by the sensor node timer. Since the packet (and data symbol) arrival time is now synchronized to the sensor node baseband timer, the sensor node receiver no longer requires power-demanding timing offset estimation and symbol boundary synchronization. The sensor receiver can simply sample and compare to demodulate the OOK-modulated signal. Note that in this scheme, it is the sensor node that periodically initiates communication with the base station, while the base station performs energy-/power-demanding synchronization. The time interval between communication initiations is set using a sleep timer [24] in the sensor node and does not need to be very accurate since the receiver is always listening. In this design, the sleep timer frequency is typically 3.5 Hz but is tunable. For the sensor node, the digital baseband controller is integrated with an on-chip 200 kHz timer, which employs a resistive frequency locking technique [21]. Thanks to the sensor-initiated synchronization scheme, the baseband controller and timer consume only a 4.8  $\mu$ W active power in total.

### C. Wakeup Scheme

Since many medical implants require long-term monitoring, battery life is critical for these applications. Fig. 6 shows the architecture and timing diagram of the wakeup system. Periodically, or as instigated by the processor, the wake-up controller powers on the 200-kHz baseband timer in two phases. First, the linear regulator inside the timer is stabilized for  $\sim$ 300 ms, while the VCO is clock gated. Then, the VCO clock gate is released, and after 7.5 k cycles for frequency stabilization, FastFSM, the finite state machine logic, clocked with the 200 kHz baseband timer, wakes up the baseband controller. This multistage wakeup is used to minimize the duration at which power-consuming blocks such as the baseband timer and the baseband controller are active, while giving lower power blocks such as the regulator enough time to stabilize. In the simulation, the regulator consumes  $\sim$ 50 nW, while the VCO consumes  $\sim$ 250 nW. However, the regulator requires a stabilization time of 300 ms, while the timer requires only a 100 ms stabilization time. Hence, the regulator is stabilized first using the sleep timer, after which the baseband timer is stabilized by counting its own clock

cycles since the sleep timer frequency is too slow to accurately set the stabilization time.

After the baseband controller is clocked and enabled, it interacts with the processor via MBUS to retrieve the message data. The baseband controller then powers on the transceiver and performs time-multiplexed modulation (TX) and demodulation (RX) according to the sensor-initiated protocol. After completing a complete cycle of TX and RX, the baseband controller raises the “BB\_DONE” signal, which switches the system back to sleep mode, with only the wake-up controller and sleep timer remaining active. The overall sleep power of SoC is measured to be 22 nW, which results from the power of wake-up controller and the sleep timer and leakage current of all other circuits and pads.

The system is designed to operate on a  $1 \times 2.2$  mm<sup>2</sup> thin-film battery (2  $\mu$ Ah, 4.1 V). Consider a periodic communication session where the sensor node wakes up and transmits and receives 16 b data. Per session, the transmitter is active for 8 ms at 43.5  $\mu$ W (2 kb/s) and receiver operates for 160  $\mu$ s at 36  $\mu$ W (100 kb/s). If the guard (or turnaround) time is 100 ms between transmit and receive phases, the baseband controller operates for 108.16 ms at 4.5  $\mu$ W. The baseband timer consumes 300 nW for 508.16 ms per session including the time for stabilization. Therefore, the total energy that the SoC consumes per session is 993 nJ. The stabilization of baseband timer is necessary because stable clock is required for synchronous communication between the sensor node and the base station. However, it adds energy overhead each time the system wakes up. The startup of the baseband timer consumes 300 nW for 400 ms, while the system sleep power is 22 nW. Thus, as long as sleep time is longer than 0.43 s, duty cycling of the baseband timer is worthwhile to save energy. The system is highly duty cycled to increase the battery life ( $\gg$ 0.43 s). Assuming a periodic session with 10 min interval, the average power of the whole system is 23.7 nW (sleep power is 22 nW). It corresponds to a 2 week expected lifetime without battery recharging.

Although the above calculation assumes no battery recharging, for final implants, wireless power transfer from an external energy source can be used to recharge the thin-film battery, which can further improve device lifetime. Typically, power can be wirelessly transferred through an inductive coupling link [25]. Other wireless transfer methods have also been proposed, including near-infrared light [26], [27] and current bursts through electrodes [28]. However, wireless power transfer using the proposed antenna is beyond the scope of this paper and the subject of future work.

## III. ANTENNA DESIGN

### A. Asymmetric Inductive Link

The target link between the sensor node and the base station is asymmetric, which results from the fact that the antenna in the base station has a relaxed dimension constraint ( $>$ cm<sup>2</sup>), whereas the sensor antenna has a strictly constrained dimension ( $<$ 1  $\times$  10 mm<sup>2</sup>) due to the size of the syringe needle. Furthermore, in the proposed system, the millimeter-scale sensor antenna is printed on glass substrate for easy assembly, while the base station antenna is printed on a circuit

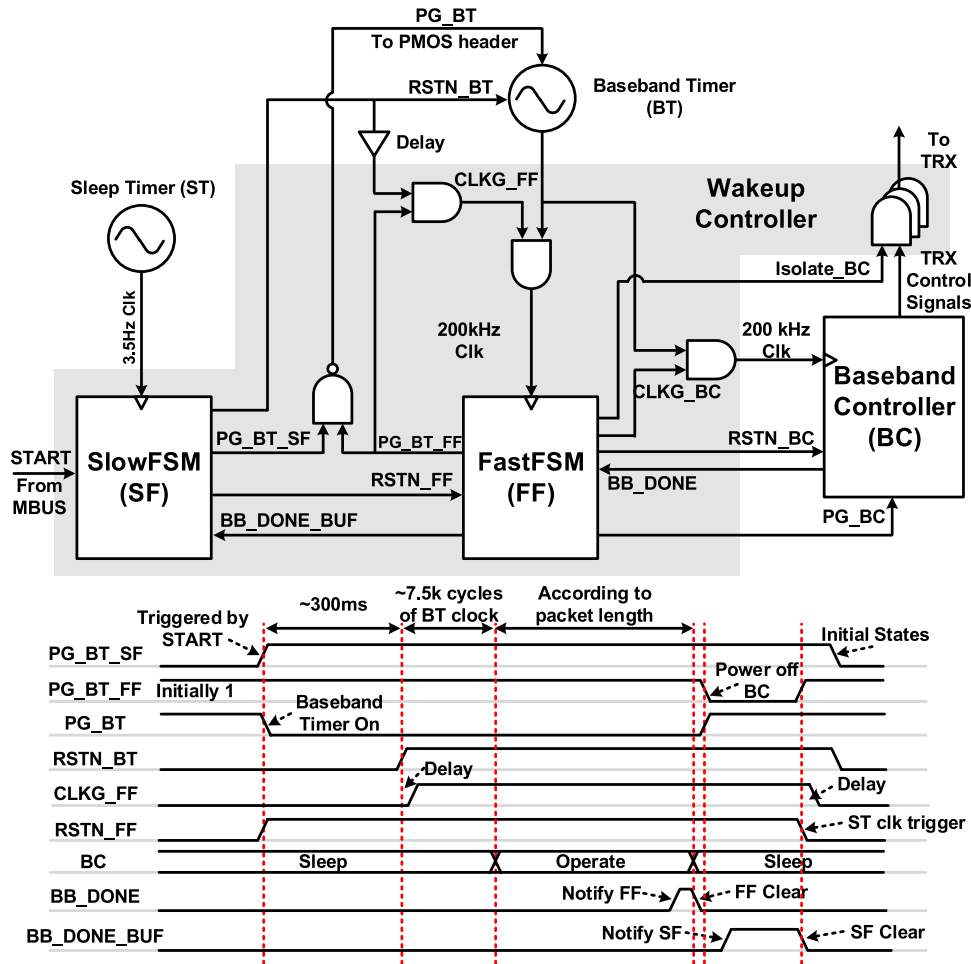


Fig. 6. Architecture and timing diagram of wakeup system.

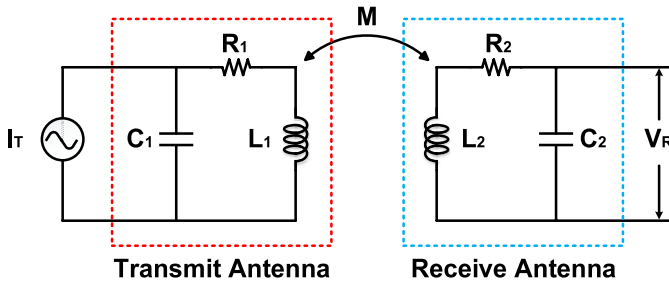


Fig. 7. Modeling of asymmetric inductive link.

board (FR4 material). The base station antenna has a relatively large quality factor ( $>60$ ) due to lower loss traces of FR4 printed board.

Most biological tissues have a magnetic permeability almost equal to that of a vacuum, which makes the inductive link suitable for through-tissue communication [29]. First-order modeling of the inductive link is shown in Fig. 7, where  $L_1$  and  $L_2$  are self-inductances,  $R_1$  and  $R_2$  are loss resistances,  $C_1$  and  $C_2$  are parallel capacitances, and  $M$  is mutual inductance. The subscripts 1 and 2 indicate the transmitting side and the receiving side, respectively. A resonant inductive link is utilized because at resonant frequency, the coupling strength is maximized due to passive voltage boosting, which

can enhance the communication range [30]. The coupling strength is quantified with transimpedance, whose magnitude at resonant frequency is

$$\left| \frac{V_R}{I_T}(\omega_s) \right| = \omega_s M Q_1 Q_2 \quad (1)$$

where  $V_R$  is the received voltage,  $I_T$  is the transmitted current,  $M$  is the mutual inductance,  $Q_1$  and  $Q_2$  are the quality factor of the each antenna, and  $\omega_s$  is the self-resonant frequency (SRF). In this paper, we design the two antennas to resonate at the same frequency, which is the theoretical optimum center frequency. Note that the coupling link in Fig. 7 is a passive two-port network, which is reciprocal and thus transfer functions are same regardless of communication direction between the implanted sensor node and the base station.

### B. Antenna Design Flow

To determine coupling strength, four variables [ $Q_1$ ,  $Q_2$ , SRF, and  $M$  (1)] must be cooptimized, and those variables are functions of the antenna dimension. In our design, High Frequency Structure Simulator (HFSS) is used to simulate an individual coil to acquire  $Q$  and SRF of each possible coil dimension. However, mutual inductance depends on the distance between

the two antennas, and simulating a complicated 3-D scenario with the two antennas in HFSS is extremely time consuming. Thus, the mutual inductance is calculated based on a model called partial element equivalent circuit (PEEC) [31]. For any two magnetic antennas, the total mutual inductance is the sum of all of the partial mutual inductances that exist between any pair of metal bars [32].

If the current distribution in each conductor is uniform (i.e., there is negligible skin effect), then the partial mutual inductance can be calculated using an equation that depends solely on the geometry and relative position of the two bars [33], which allows for extremely fast mutual inductance calculation, which implemented in MATLAB. While the PEEC does not model retardation, this is an acceptable approximation for near-field communication and the resulting accuracy is within 3% compared with the 3-D HFSS simulation.

Using the two analysis tools PEEC and HSFF, the overall antenna optimization is then performed as follows: a particular set of antenna dimensions is selected. The sensor and base station antennas are each individually simulated using HFSS to obtain  $Q$  and SRF, and then the MATLAB PEEC model is used to obtain  $M$ . These model parameters are then inserted into the model equation to obtain the transimpedance or in the model itself to perform cosimulation with the transceiver circuits.

Since each of the two antennas has three parameters (outer width  $W$ , outer length  $L$ , and number of turns  $N$ ), the number of possible antenna topologies is enormous. To make this multidimensional search tractable, we first constrain the total width of the sensor antenna to 1 mm to fit in the syringe diameter, leaving two search parameters for the sensor antenna ( $L_{sn}$  and  $N_{sn}$ ). Second, we assume that base station antenna is square shape ( $W_{bs} = L_{bs}$ ), leaving two parameters for the base station antenna ( $W_{bs}$  and  $N_{bs}$ ). To further limit the search space, we make a useful observation that a single-turn base station antenna is optimal, as shown in Fig. 8, because as the number of turns is reduced, the SRF and  $Q$  of the base station antenna increase, while  $M$  decreases. At the same time, the corresponding optimal sensor antenna also has a higher  $Q$  due to the increased frequency. Since three factors ( $\omega_s$ ,  $Q_1$ , and  $Q_2$ ) increase and one ( $M$ ) decreases when the fill factor is reduced, a smaller turn number results in a larger transimpedance. Therefore, we arrived at the conclusion that a single-turn base station antenna is optimal ( $N_{bs} = 1$ ). This reduces the number of search parameters to only three ( $W_{bs}$ ,  $L_{sn}$ , and  $N_{sn}$ ). In this derivation, the metal width and spacing of the PCB antenna are 600 and 250  $\mu\text{m}$ , respectively, which are chosen to constrain the searching space. Fill factor in Fig. 8 is calculated based on this width, spacing, the turn number, and outer dimension. If further optimization is desired, the metal width and spacing should also be taken into consideration in the design process.

The final antenna dimension search is then performed as follows. For each sensor antenna length and number of turns, the optimal corresponding base station antenna (with a certain outer dimension) is found by matching its SRF with that of the sensor antenna SRF. The resulting antenna configuration is then analyzed, the transimpedance is obtained and the

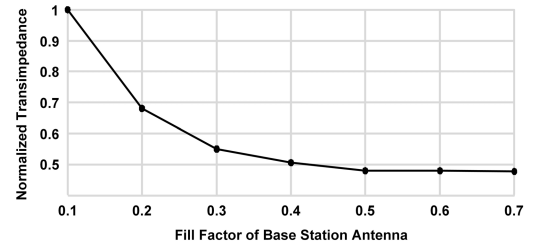


Fig. 8. Relationship between coupling strength and fill factor of the base station antenna.

optimal configuration is selected. Fig. 9(a) shows the model parameters versus sensor antenna length and the resulting transimpedance. Increasing the sensor antenna length results in monotone increasing transimpedance due to increasing mutual inductance. However, beyond an 8 mm length, transimpedance saturates due to decreasing  $Q$  and SRF, and thus there is a diminishing return for increased size. We also found a similar tradeoff for the fill factor, which is shown in Fig. 9(b). The transimpedance saturates when the fill factor is larger than 0.6, which corresponds to 15 turns. Thus, the sensor antenna is designed to be  $1 \times 8 \text{ mm}^2$  in total size with 15 turns of 15  $\mu\text{m}$  turn width and 5  $\mu\text{m}$  spacing, while the corresponding single-turn PCB antenna is  $11 \times 11 \text{ cm}^2$  with 600  $\mu\text{m}$  metal width. The layout of sensor antenna and the photo of base station antenna are shown in Fig. 10(a) and (b) respectively. The sensor antenna was simulated in HFSS and measured with probe testing, as shown in Fig. 10(c) and (d). We used impedance standard substrates to calibrate the network analyzer and probe setup, which decouples the effect of probe in testing and ensures accuracy. At the chosen frequency, the skin depth within the gold metal is 7.2  $\mu\text{m}$ , which is comparable with the half metal width (15  $\mu\text{m}$ ) and larger than the metal thickness (1.5  $\mu\text{m}$ ) of sensor antenna. Therefore, skin effect is expected to be small in the proposed antenna structure.

### C. Frequency Selection

In this paper, the 114.7 MHz center frequency for uplink from the sensor node to the base station is determined based on the above analysis to maximize the link strength. At this particular center frequency, the field strength due to the signal transmitted from the sensor node remains well below the FCC limit of 150  $\mu\text{V/m}$  at a distance of 3 m [34] since the sensor antenna has very limited gain. However, this FCC spectral mask significantly constrains the maximum power from the base station, while a large base station transmit power is desired to relax the sensitivity requirement of the sensor receiver. As a solution, we propose a system with asymmetric center frequency allocation. We observe that the FCC limit at 49.82–49.9 MHz is 36.5 dB larger than 150  $\mu\text{V/m}$ , allowing base station to transmit 36.5 dB larger power in this band. However, the resulting transimpedance is 21.5 dB weaker due to lower frequency and lower resonant  $Q$  for the designed antenna pair. Overall, the requirement for sensor node sensitivity is reduced by 15 dB. Therefore, we selected 49.86 MHz as the center frequency for the base station to sensor, even if it is suboptimal in terms of link strength. We implement a digitally tunable on-chip capacitor array to change the sensor

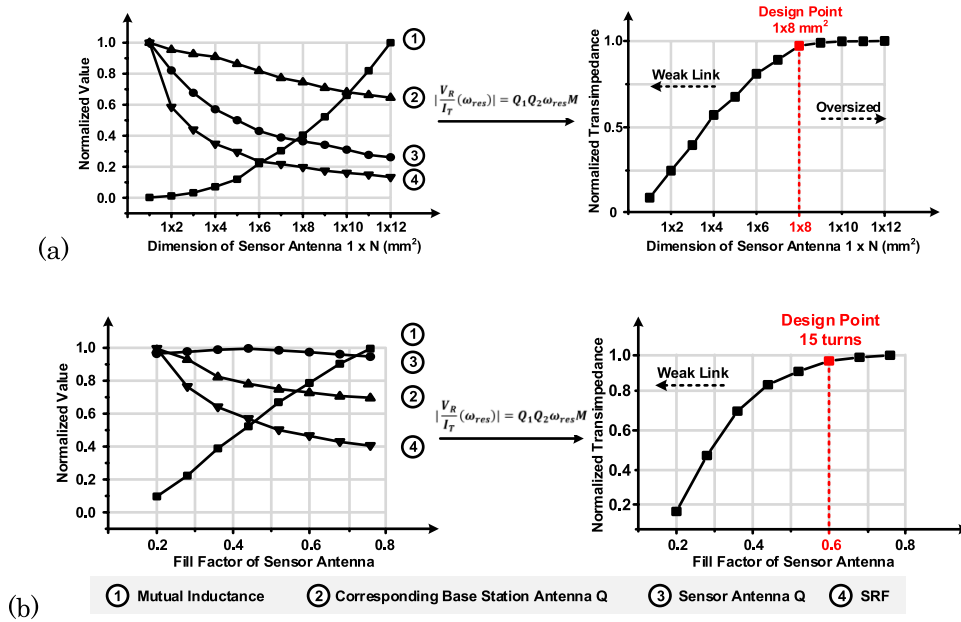


Fig. 9. Codesign of the sensor antenna with base station antenna in terms of (a) dimension and (b) fill factor.

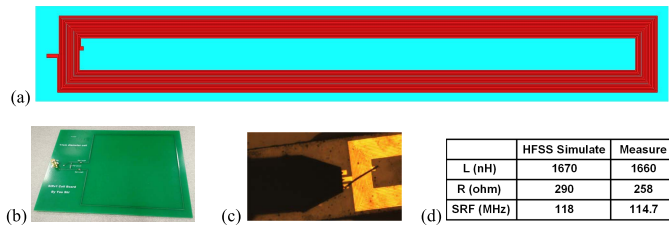


Fig. 10. (a) Layout of sensor antenna on glass substrate. (b)  $11 \times 11 \text{ cm}^2$  base station antenna printed on FR4 board. (c) Probe testing of sensor antenna. (d) Comparison of HFSS simulation and measurement results for sensor antenna.

node antenna resonant frequency according to the transmit and receive modes.

#### D. Effect of Biological Tissue

Until now, proposed design flow has not considered the effect from biological tissue after implantation. However, it can be expected that resonant frequency of antenna may change due to the tissue around it. HFSS simulation shows that the resonant frequency of sensor antenna will shift down by 12 MHz when the antenna is packaged by a  $1 \times 1 \times 10 \text{ mm}^3$  glass capsule and fully covered by a muscle tissue. The frequency-dependent dielectric properties of the muscle are based on [35]. The frequency shift can be tolerable in this paper, since the base station transceiver has the ability to tune carrier frequency.

### IV. CIRCUIT DESIGN

#### A. Pulsed Transmitter

Fig. 11 shows the architecture of the transmitter and the associated conceptual waveforms. The transmitter consists of a power oscillator, a pulse generator, a current limiter, and a decoupling capacitor (decap). The power oscillator, combining

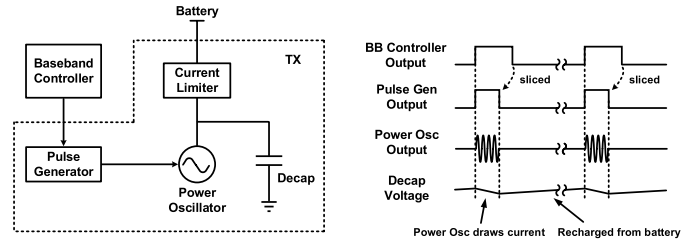


Fig. 11. Architecture of pulsed transmitter and conceptual waveforms.

the functions of frequency generation and power delivery, is implemented to replace the power-hungry frequency synthesizer and power amplifier. The sensor transmitter circuit operates at 13.6 mW for the maximum output power. However, the maximum peak power of the intended thin-film battery ( $< 50 \mu\text{W}$ ) is insufficient to provide such a large current to power the oscillator. Thus, we employ an integrated decap (1.3 nF) made of a metal–insulator–metal (MIM) capacitor as an energy buffer. The decap is formed by top two metal layers, which are placed over digital circuits (wakeup controller, baseband controller, and MBUS controller) to save chip area. As shown in Fig. 11, during a pulse, the power oscillator draws high current from the decap (decap voltage drops), delivering strong output power to the antenna. After a pulse is transmitted, the power oscillator is shut down and the decap needs to be recharged before the next pulse is transmitted. However, the peak current that can be drawn from the battery is limited by its large intrinsic resistance. In this paper, the current limiter is implemented as a series resistor ( $\sim 100 \text{ k}\Omega$ ) between the battery and the decap, limiting the recharging current to be less than  $15 \mu\text{A}$ , which protects the battery from being overdrawn. Therefore, the recharging time is long compared with the pulse width and the resulting transmitted signal is a series of sparse pulses. To exploit this unique feature, the transmitter employs

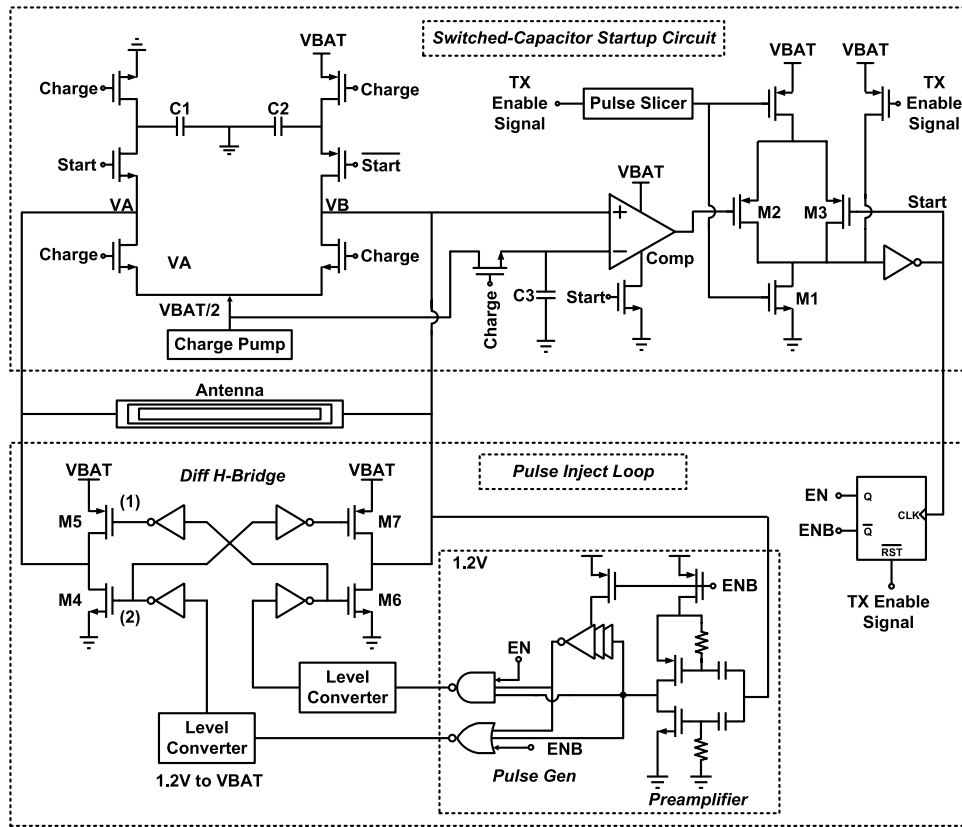


Fig. 12. Schematic of proposed PIO.

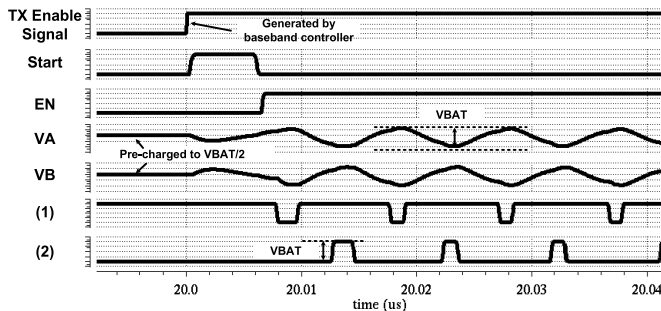


Fig. 13. Simulated waveforms of PIO using SPICE.

pulse position modulation. The baseband controller generates the control signals to enable the pulse TX. The “enable” signal is sliced by the pulse generator to produce a tunable width pulse, which can be shorter than a baseband clock period.

A conventional power oscillator is based on a cross-coupled pair of oscillators that provide negative resistance. To start up and sustain the oscillation, the negative resistance, which depends on the bias current, must be large enough to overcome the loss in the tank [15], [36]. However, since the oscillator draws constant bias current, it has a low transmit efficiency (simulated as 40%). In this paper, we propose a new pulse-inject oscillator (PIO). Fig. 12 shows its schematic, which consists of a switched-capacitor start-up circuit and a pulse-inject loop. To increase efficiency, the proposed oscillator injects pulsed current through an H-bridge only when oscillation is near the peak. The startup time, a critical factor for an efficient pulsed radio, is less than two cycles.

Fig. 13 shows the simulated waveforms in SPICE, showing the operation of the PIO. Before a pulse is generated, it takes 20  $\mu$ s to “precharge” (charge = 1, TX\_EN = 0), with C1 discharged to ground and C2 charged to VBAT. At the same time, the two nodes of the antenna (VA and VB) are charged to VBAT/2, which is the desired common mode voltage. C3 is also charged to VBAT/2, which will be used as the reference voltage in the next phase. Note that “Start” is zero, so the open-loop comparator is OFF. VBAT/2 is generated using a series-parallel charge pump, clocked by the baseband timer. After “precharging” is finished, TX\_EN toggles to one and the pulse slicer generates a pulse of  $\sim$ 1.2 ns, which turns on nMOS footer M1 and switches “Start” to one. When “Start” becomes one, C1 and C2 share charge with the antenna and inject an initial charge to VA and VB, initiating oscillation. Since “Start” is one, the comparator is powered on and its output is one. When the pulse slicer output returns to zero, M1 is turned off, but “Start” remains one because the pMOS switches M2 and M3 are OFF. VA and VB continue to change until half of an oscillation cycle is completed. Since VB crosses VBAT/2, the output of the comparator toggles from 1 to 0, switching “Start” to 0 and causing three things to happen. First, C1 and C2 are disconnected from the antenna since enough energy is now transferred into the antenna. Second, the comparator is powered off. Third, the pulse-inject loop is enabled by a negative-edge triggered flip-flop. At this point, the pulse-inject loop sustains the oscillation. A preamplifier combined with a pulse generator extracts and generates digital pulses from the oscillation signal. The preamplifier uses resistor bias at

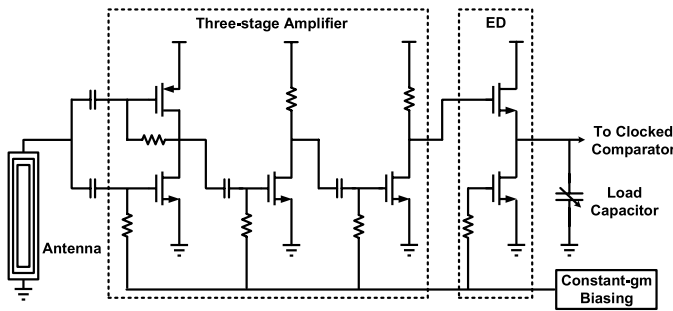


Fig. 14. Schematic of OOK receiver.

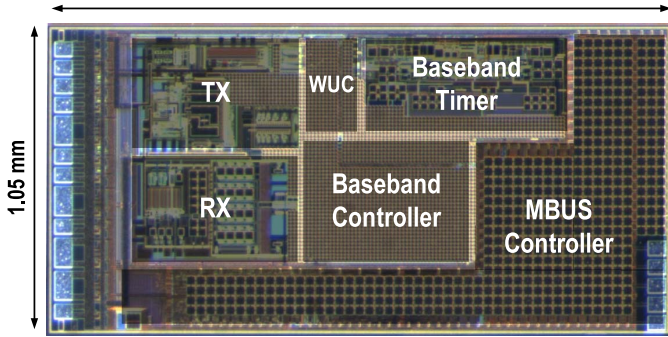


Fig. 15. Die photograph of the proposed radio, where MIM decoupling capacitor is placed over WUC, baseband controller, and MBUS controller.

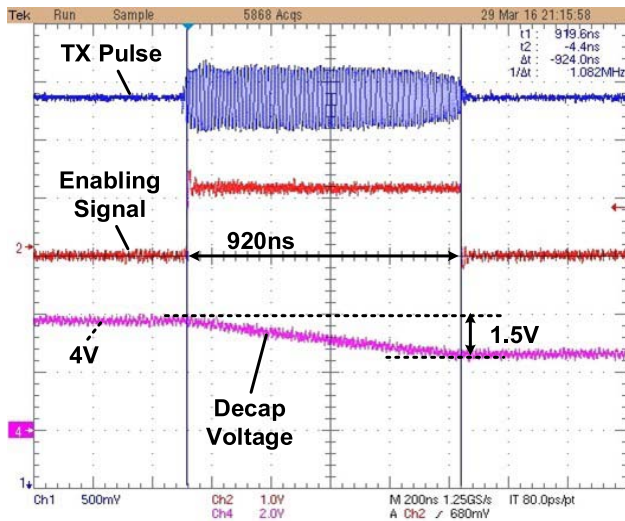


Fig. 16. Measured waveforms of transmitter.

its gates to reduce short-circuit current. The pulses at the transistor gates of the differential H-bridge, which are tuned to overlap with the peak of the oscillation points, control the H-bridge to inject current into the antenna differentially, which sustains the oscillation. The four transistors (M4–M7) have low power loss because during current injection,  $V_{DS}$  is low, and during off-state, the current is 0, which enhances efficiency. The proposed design utilizes two voltage domains (1.2 V and 4.1 V  $V_{BAT}$ ) to reduce the overall power consumption. During a pulse, VA and VB oscillate at full swing between 0 and the battery voltage (4.1 V), which provides

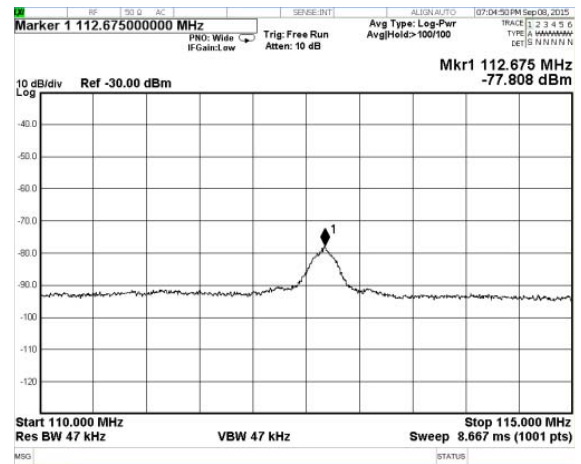


Fig. 17. Measured power spectrum of transmitted signal received by base station antenna.

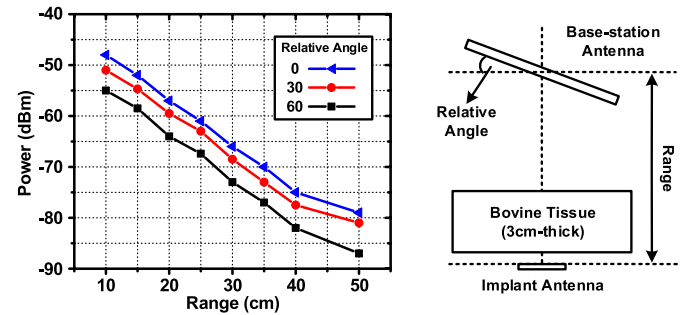


Fig. 18. Measured transmitter output power versus range and relative angle between two antennas.

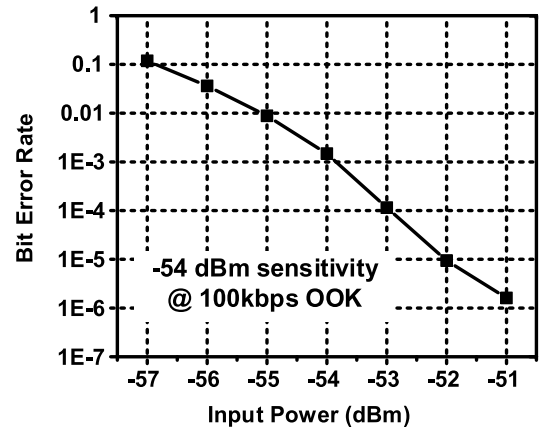


Fig. 19. Measured sensitivity of receiver.

the largest possible transmit power. The simulated power efficiency of the proposed PIO is 68%, which is  $1.65\times$  higher than that of a constant-bias cross-coupled oscillator. Since the battery voltage ( $V_{BAT}$ ) is 4.1 V, high threshold voltage transistors with thick gate oxide are utilized for the circuits that operate on battery voltage and standard threshold voltage transistors are used for 1.2 V domain.

*B. OOK Receiver*

Unlike the sensor node where pulsed TX is employed because of the power constraint, the base station transmits with

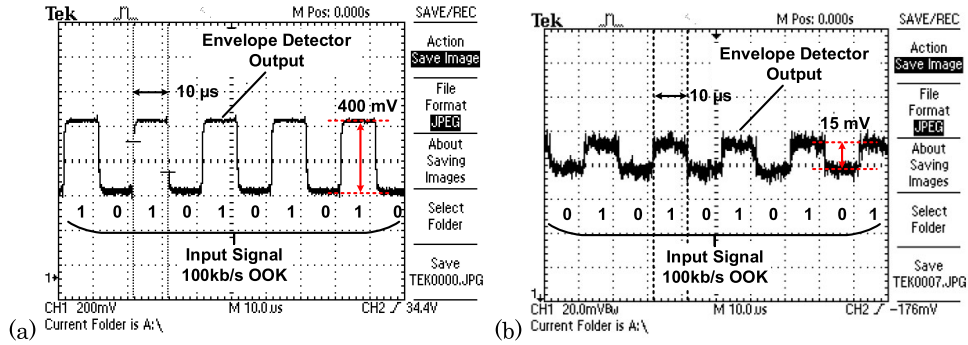


Fig. 20. Measured waveforms at the output of receiver ED wirelessly at the distances of (a) 3 cm and (b) 20 cm.

a continuous OOK scheme. The sensor receiver demodulates the OOK signal from the base station continuously drawing current from the 1.2 V supply. It is feasible because its power consumption is less than the maximum peak power of the millimeter-scale battery ( $<50 \mu\text{W}$ ). Fig. 14 shows the schematic of the receiver, which consists of a three-stage amplifier, envelope detector (ED), and clocked comparator. The received signal is amplified and demodulated by the ED. A clocked comparator samples and digitizes the output of the ED.

The first-stage amplifier is a current-reuse inverter amplifier for high current efficiency. The transistors in the amplifier are biased at the subthreshold region for higher  $g_m/I$  efficiency. The gain of the three-stage amplifier is simulated as 37 dB at 49.86 MHz. The ED comprises a source follower topology, and the transistor is biased at the nonlinear region, consuming  $\sim 200 \text{ nA}$ . The load capacitor can be tunable up to 31 pF, filtering out any high frequency components. A constant- $g_m$  biasing circuit is designed for the amplifier and ED. The total receiver consumes  $36 \mu\text{W}$  while demodulating a 100 kb/s OOK signal.

## V. MEASUREMENT RESULTS

Fig. 15 shows the chip microphotograph of the proposed near-field radio fabricated in a 180 nm CMOS technology. The chip has a total area of  $1050 \mu\text{m} \times 2120 \mu\text{m}$  including the pads. Proposed radio is designed for wireless through-tissue communication. To demonstrate this feasibility, a medium of 3-cm-thick bovine tissue (typical beef steak) is utilized by following the wireless testing of the transceiver.

The transmitter was measured when driving the antenna on the glass substrate (sensor antenna). Fig. 16 shows the measured time-domain waveforms of the transmitter in pulsed mode. Once the pulse is enabled by the baseband controller, the oscillation can start up quickly. With the pulse generator, the pulse width can be digitally tunable from 150 to 1320 ns. When the pulse width is 920 ns, the transmitter supply voltage on the decap drops by 1.5 V during every pulse as shown in the measurement but is recharged to its full level after  $\sim 500 \mu\text{s}$ , where the current limiter sets the recharging current to be less than  $15 \mu\text{A}$ . For the communication range and power spectrum measurement setup, we used an external 4.1 V supply to allow the sensor node power oscillator to continuously draw current. The sensor transmitted signal was

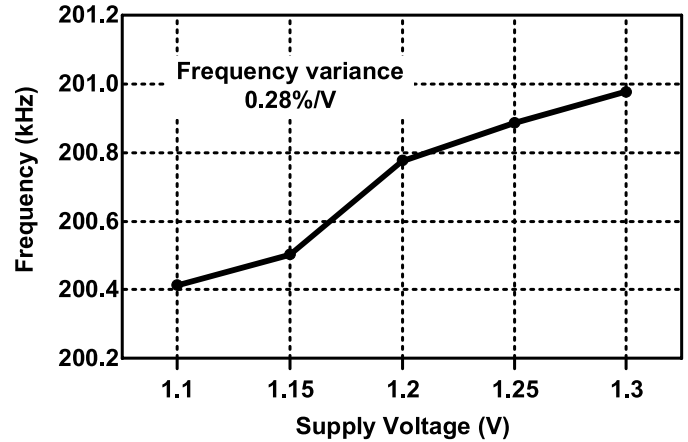


Fig. 21. Measured supply variance of baseband timer frequency.

wirelessly received by the  $11 \times 11 \text{ cm}^2$  base station loop antenna printed on an FR4 board through a 3-cm-thick bovine tissue. Fig. 17 shows the power spectrum measured with a spectrum analyzer, and Fig. 18 shows the measured power across a range of distances and relative angles between the two antennas. The receiver sensitivity was measured using a wired setup where an RF signal generator was connected to the sensor node receiver via a cable or through the antenna pair. The wired setup is used to measure receiver sensitivity quantitatively, where the input of the receiver was connected to the signal generator (source  $50 \Omega$ ) through an SMA cable. Fig. 19 shows the measured sensitivity across input power, which is the value directly read from the signal generator. Note that due to impedance mismatch (receiver input non- $50 \Omega$ ), actual receiver input power is less than the value read from the signal generator. At a BER of  $10^{-3}$  and a data rate of 100 kb/s, the receiver has a sensitivity at  $-54 \text{ dBm}$  and consumes  $36 \mu\text{W}$  at a supply voltage of 1.2 V. This same BER was also measured wirelessly at approximately 20 cm through the 3 cm-thick bovine tissue, where the RF signal generator feeds the OOK-modulated signal into the base station antenna with a 1 W power and the chip detects it using the sensor antenna. While demodulating a 100 kb/s OOK signal, the measured waveforms of the ED output when the two antennas are separated by 3 and 20 cm are shown in Fig. 20(a) and (b), respectively.

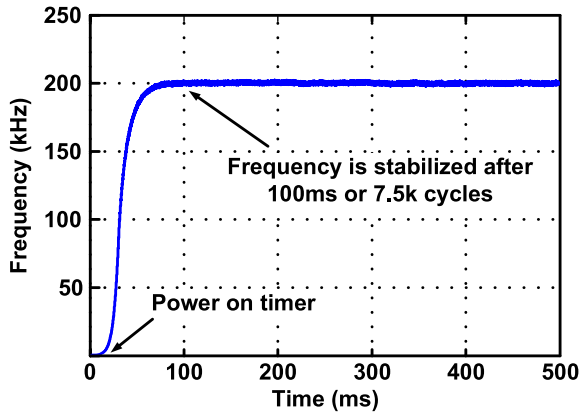
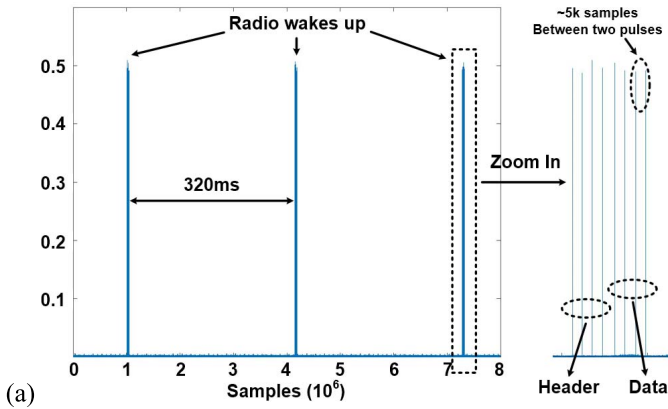
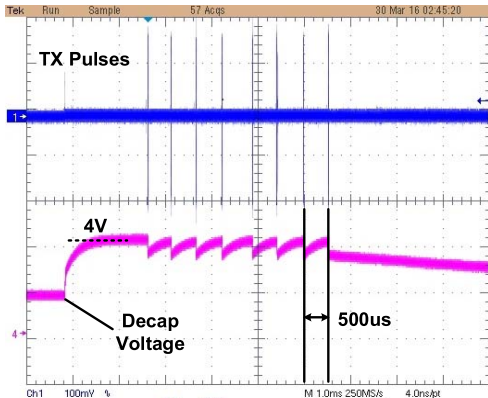


Fig. 22. Measured transient settling of baseband timer frequency.



(a)



(b)

Fig. 23. (a) Captured transmitted pulses using prototype base station receiver. (b) Measured waveforms of transmitter showing correspondence.

The timer has a nominal frequency of approximately 200 kHz. Since the temperature is typically stable in implanted applications, the frequency variance of the timer is dominated by the supply variation. Fig. 21 shows the measured frequency variance with the supply voltage ranging from 1.1 to 1.3 V, corresponding to a supply variation of 0.28%/V. Fig. 22 shows the transient response of the timer frequency after powering on the timer, demonstrating that the frequency is stabilized after 7.5 k clock cycles, which is approximately 100 ms.

To demonstrate the proposed radio system, we implemented a prototype base station that can detect the transmitted pulses

TABLE I  
SUMMARY OF THE SYSTEM PERFORMANCE

<b>Technology</b>		<b>180nm CMOS</b>
<b>Die Area</b>		<b>2.12 x 1.05 mm<sup>2</sup></b>
<b>Transmitter</b>	<b>Average Power</b>	<b>43.5 μW @ 4.1V</b>
	<b>Peak Power</b>	<b>13.6 mW @ 4.1V</b>
	<b>Center Frequency</b>	<b>112 MHz</b>
	<b>Modulation</b>	<b>PPM</b>
	<b>Pulse Width</b>	<b>150-1320 ns</b>
	<b>Data Rate</b>	<b>2 kbps</b>
<b>Output Power</b>		<b>-78 dBm @ 50cm</b>
<b>Receiver</b>	<b>Active Power</b>	<b>36 μW @ 1.2V</b>
	<b>Center Frequency</b>	<b>49.86 MHz</b>
	<b>Modulation</b>	<b>OOK</b>
	<b>Data Rate</b>	<b>100 kbps</b>
	<b>Sensitivity</b>	<b>-54 dBm</b>
	<b>BER</b>	<b>10<sup>-3</sup></b>
<b>Baseband</b>	<b>Active Power</b>	<b>4.8 μW @ 1.2V</b>
	<b>Clock Frequency</b>	<b>200 kHz</b>
<b>System Sleep Power (Including Wake-up Controller)</b>		<b>22 nW</b>

from the proposed radio by downmixing, converting to the digital format, and oversampling at 10 MHz. Fig. 23(a) shows the captured pulses using the prototype base station. It shows that the proposed radio is woken up every 320 ms (programmable) by the wakeup controller. Every time the radio wakes up, it transmits a packet consisting of eight pulses. Fig. 23(b) shows the measured waveforms of the transmitted pulses and the decap voltage. After the radio wakes up, the decap is charged to 4 V and the transmitter generates pulses, which are controlled by the baseband controller. After TX finishes, transmitter circuits are power gated and the decap is disconnected from the battery, and thus the decap voltage gradually drops due to leakage current, as expected. The generated pulse pattern corresponds with the captured results at the base station. When 32 pulses are used for the packet header, the software-based algorithm on the base station can successfully track and correct the baseband frequency offset within 2000 ppm (0.2%) between the sensor node and the base station.

To demonstrate a complete self-contained system, this radio chip is measured with other system peripherals including a processor layer, a decap layer, and the power management unit [19]. During the testing, the battery voltage (4 V) is provided from a supply generator, while 1.2 V voltage is generated by the power management unit by downconverting from the same 4 V terminal. Configured by the processor on the processor layer using the MBUS interlayer communication [17], the chip periodically wakes up, transmits and receives data as expected, verifying the functionality of the power management scheme and chip-to-chip interface. Table I summarizes the performance of each block in the radio. Table II provides a comparison with related prior work.

TABLE II  
COMPARISON WITH RECENT PRIOR WORK

		This Work	CICC 2013 [13]	ISSCC 2011 [15]	VLSI 2011 [12]
<b>Technology</b>		180 nm	65 nm	180 nm	65 nm
<b>Application</b>		Syringe-implanted Sensors	Implanted Sensors	Intraocular Pressure Monitor	Implanted Neural Sensor
<b>Antenna</b>		1 x 8 mm <sup>2</sup> 15-turn	2 x 2 mm <sup>2</sup> 1-turn	0.4 x 0.4 mm <sup>2</sup> 6-turn	1.1 x 1.1 mm <sup>2</sup> 1-turn
<b>Communicate Distance</b>	<b>Transmit</b>	50 cm	3.5 cm	10 cm	1.3 cm
	<b>Receive</b>	20 cm	3.5 cm	N/A	N/A
<b>Transmitter</b>	<b>Architecture</b>	Pulse Injection LC Oscillator	Passive	Constant Bias LC Oscillator	Passive
	<b>Center Freq</b>	112 MHz	1.32–2.14 GHz	570/690 MHz	535 MHz
	<b>Modulation</b>	PPM	LSK	FSK	LSK + PPM
	<b>Peak Power</b>	13.6 mW	1.4 μW	45.7 mW	660 nW
	<b>Data Rate</b>	2 kbps	2 Mbps	7.5 kbps	2 Mbps
<b>Receiver</b>	<b>Sensitivity</b>	-54 dBm @ 100kbps	Unknown	N/A	N/A
	<b>BER</b>	1x10 <sup>-3</sup>	Unknown		
	<b>Center Freq</b>	49.86 MHz	1.32–2.14 GHz		
	<b>Modulation</b>	OOK	ASK		
	<b>Power</b>	36 μW	1.2 μW		
<b>Baseband Controller and Clock</b>		Integrated	N/A	N/A	N/A

## VI. CONCLUSION

A fully integrated near-field radio chip fabricated in a 180 nm CMOS technology is demonstrated for syringe-implantable smart sensor nodes. A 1 × 8 mm<sup>2</sup> antenna printed on a glass substrate and an 11 × 11 cm<sup>2</sup> base station antenna printed on an FR4 circuit board are codesigned to form an asymmetric inductive link between the sensor node and base station. The transceiver, codesigned with the 1 × 8 mm<sup>2</sup> sensor antenna, consumes a 43.5 μW average power at 2 kb/s, while the receiver power consumption is 36 μW with a -54 dBm sensitivity at 100 kb/s. The radio can operate on a millimeter-scale battery that has a stringent 50 μW peak power constraint. The system was measured to achieve a range of 50 cm for the sensor TX and 20 cm for RX. This paper enables wireless communication for the implanted smart devices, increasing their potential use cases in healthcare applications.

## REFERENCES

- [1] V. Reddy *et al.*, "Percutaneous implantation of an entirely intracardiac leadless pacemaker," *New England J. Med.*, vol. 373, no. 12, pp. 1125–1135, Sep. 2015.
- [2] F.-G. Zeng, S. Rebscher, W. V. Harrison, X. Sun, and H. Feng, "Cochlear implants: System design, integration, and evaluation," *IEEE Rev. Biomed. Eng.*, vol. 1, pp. 115–142, Nov. 2008.
- [3] I. H. Lee, "Power management circuits for miniature sensor systems," Ph.D. dissertation, Dept. Elect. Eng., Univ. Michigan, Ann Arbor, MI, USA, 2014.
- [4] VeriTeQ Corp. *Implantable Microchip and Patient Identification*, accessed on Sep. 2016. [Online]. Available: <http://divpixel.net/veriteq/patientId.html>
- [5] G. E. Loeb, R. A. Peck, W. H. Moore, and K. Hood, "BION system for distributed neural prosthetic interfaces," *Med. Eng. Phys.*, vol. 23, pp. 9–18, Jan. 2001.
- [6] B. Ziaie, M. D. Nardin, A. R. Coghlan, and K. Najafi, "A single-channel implantable microstimulator for functional neuromuscular stimulation," *IEEE Trans. Biomed. Eng.*, vol. 44, no. 10, pp. 909–920, Oct. 1997.
- [7] P. R. Troyk, "Injectable electronic identification, monitoring, and stimulation systems," *Annu. Rev. Biomed. Eng.*, vol. 1, no. 1, pp. 177–209, Aug. 1999.
- [8] Y. Lee *et al.*, "A modular 1 mm<sup>3</sup> die-stacked sensing platform with low power I<sup>2</sup>C inter-die communication and multi-modal energy harvesting," *IEEE J. Solid-State Circuits*, vol. 48, no. 1, pp. 229–243, Jan. 2013.
- [9] M. Fojtik *et al.*, "A millimeter-scale energy-autonomous sensor system with stacked battery and solar cells," *IEEE J. Solid-State Circuits*, vol. 48, no. 3, pp. 801–813, Mar. 2013.
- [10] Y.-P. Chen *et al.*, "An injectable 64 nW ECG mixed-signal SoC in 65 nm for arrhythmia monitoring," *IEEE J. Solid-State Circuits*, vol. 50, no. 1, pp. 375–390, Jan. 2015.
- [11] Cymbet Corp. *EnerChip Smart Solid State Batteries*, accessed on Sep. 2016. [Online]. Available: <http://www.cymbet.com/products/enerchip-solidstate-batteries.php>
- [12] M. Mark *et al.*, "A 1 mm<sup>3</sup> 2 Mbps 330 fJ/b transponder for implanted neural sensors," in *Proc. IEEE Symp. VLSI Circuits*, Jun. 2011, pp. 168–169.
- [13] A. Yakovlev, J. Jang, D. Pivonka, and A. Poon, "A 11 μW sub-pJ/bit reconfigurable transceiver for mm-sized wireless implants," in *Proc. IEEE Custom Integr. Circuits Conf.*, Sep. 2013, pp. 1–4.
- [14] A. Shirane *et al.*, "RF-powered transceiver with an energy- and spectral-efficient IF-based quadrature backscattering transmitter," *IEEE J. Solid-State Circuits*, vol. 50, no. 12, pp. 2975–2987, Dec. 2015.
- [15] G. Chen *et al.*, "A cubic-millimeter energy-autonomous wireless intraocular pressure monitor," in *ISSCC Dig. Tech. Papers*, Feb. 2011, pp. 310–311.
- [16] J. L. Bohorquez, J. L. Dawson, and A. P. Chandrakasan, "A 350 μW CMOS MSK transmitter and 400 μW OOK super-regenerative receiver for medical implant communications," *IEEE J. Solid-State Circuits*, vol. 44, no. 4, pp. 1248–1259, Apr. 2009.

- [17] G. Kim *et al.*, "A millimeter-scale wireless imaging system with continuous motion detection and energy harvesting," in *Proc. IEEE Symp. VLSI Circuits*, Jun. 2014, pp. 1–2.
- [18] Y. Shi *et al.*, "A 10 mm<sup>3</sup> syringe-implantable near-field radio system on glass substrate," in *IEEE ISSCC Dig. Tech. Papers*, Feb. 2016, pp. 448–449.
- [19] W. Jung *et al.*, "A 60%-efficiency 20 nW–500  $\mu$ W tri-output fully integrated power management unit with environmental adaptation and load-proportional biasing for IoT systems," in *ISSCC Dig. Tech. Papers*, Jan./Feb. 2016, pp. 154–155.
- [20] Epson Corp., *Crystal kHz Range/Crystal Unit*, accessed on Sep. 2016. [Online]. Available: [http://www5.epsondevice.com/en/products/khz\\_range/](http://www5.epsondevice.com/en/products/khz_range/)
- [21] M. Choi, S. Bang, T.-K. Jang, D. Blaauw, and D. Sylvester, "A 99 nW 70.4 kHz resistive frequency locking on-chip oscillator with 27.4 ppm/ $^{\circ}$ C temperature stability," in *Proc. IEEE Symp. VLSI Circuits*, Jun. 2015, pp. C238–C239.
- [22] K.-K. Huang *et al.*, "An ultra-low-power 9.8 GHz crystal-less UWB transceiver with digital baseband integrated in 0.18  $\mu$ m BiCMOS," *IEEE J. Solid-State Circuits*, vol. 48, no. 12, pp. 3178–3189, Dec. 2013.
- [23] N. E. Roberts *et al.*, "A 236 nW –56.5 dBm-sensitivity Bluetooth low-energy wakeup receiver with energy harvesting in 65 nm CMOS," in *ISSCC Dig. Tech. Papers*, Feb. 2016, pp. 450–451.
- [24] I. Lee, D. Sylvester, and D. Blaauw, "A constant energy-per-cycle ring oscillator over a wide frequency range for wireless sensor nodes," *IEEE J. Solid-State Circuits*, vol. 51, no. 3, pp. 697–711, Mar. 2016.
- [25] J. S. Ho *et al.*, "Wireless power transfer to deep-tissue microimplants," *Proc. Nat. Acad. Sci. USA*, vol. 111, no. 22, pp. 7974–7979, Apr. 2014.
- [26] A. Abdo, M. Sahin, D. S. Freedman, E. Cevik, P. S. Spuhler, and M. S. Unlu, "Floating light-activated microelectrical stimulators tested in the rat spinal cord," *J. Neural Eng.*, vol. 8, no. 5, p. 056012, Sep. 2011.
- [27] K. Mathieson *et al.*, "Photovoltaic retinal prosthesis with high pixel density," *Nature Photon.*, vol. 6, pp. 391–397, May 2012.
- [28] A. Ivorra, L. Becerra-Fajardo, and Q. Castellví, "In vivo demonstration of injectable microstimulators based on charge-balanced rectification of epidermally applied currents," *J. Neural Eng.*, vol. 12, no. 6, p. 066010, Oct. 2015.
- [29] R. Pethig and D. B. Kell, "The passive electrical properties of biological systems: Their significance in physiology, biophysics and biotechnology," *Phys. Med. Biol.*, vol. 32, no. 8, p. 933, Aug. 1987.
- [30] S. W. Han, "Wireless interconnect using inductive coupling in 3D-ICs," Ph.D. dissertation, Dept. Elect. Eng., Univ. Michigan, Ann Arbor, MI, USA, 2012.
- [31] K. Gala, D. Blaauw, J. Wang, V. Zolotov, and M. Zhao, "Inductance 101: Analysis and design issues," in *Proc. 38th Annu. Design Autom. Conf.*, Jun. 2001, pp. 329–334.
- [32] H. M. Greenhouse, "Design of planar rectangular microelectronic inductors," *IEEE Trans. Parts, Hybrids, Packag.*, vol. PHP-10, no. 2, pp. 101–109, Jun. 1974.
- [33] C. Hoer and C. Love, "Exact inductance equations for rectangular conductors with applications to more complicated geometries," *J. Res. Nat. Bureau Standards*, vol. 69C, no. 2, Apr./Jun. 1965.
- [34] (Oct. 1993). *Federal Communications Commission, Understanding the FCC Regulations for Low-power, Non-Licensed Transmitters*. [Online]. Available: [https://transition.fcc.gov/Bureaus/Engineering\\_Technology/Documents/bulletins/oet63/oet63rev.pdf](https://transition.fcc.gov/Bureaus/Engineering_Technology/Documents/bulletins/oet63/oet63rev.pdf)
- [35] S. Gabriel, R. W. Lau, and C. Gabriel, "The dielectric properties of biological tissues: III. Parametric models for the dielectric spectrum of tissues," *Phys. Med. Biol.*, vol. 41, no. 11, p. 2271, Nov. 1996.
- [36] P. P. Mercier, S. Bandyopadhyay, A. C. Lysaght, K. M. Stankovic, and A. P. Chandrakasan, "A sub-nW 2.4 GHz transmitter for low data-rate sensing applications," *IEEE J. Solid-State Circuits*, vol. 49, no. 7, pp. 1463–1474, Jul. 2014.



**Yao Shi** (S'14) received the B.S. degree in electronic and information engineering from Zhejiang University, Hangzhou, China, in 2013, and the M.S. degree in electrical engineering from the University of Michigan, Ann Arbor, MI, USA, in 2016, where he is currently pursuing the Ph.D. degree.

His current research interests include analog/RF integrated circuits design, ultralow power radio architecture and circuit, and ultralow power wireless sensor node.



wireless sensor node.

Mr. Choi was a recipient of the Doctoral Fellowship from Kwanjeong Educational Foundation, South Korea.



**Myungjoon Choi** (S'12) received the B.S. degree (*summa cum laude*) in electrical engineering from the Korea Advanced Institute of Science and Technology, Daejeon, South Korea, in 2012, and the M.S. degree in electrical engineering from the University of Michigan, Ann Arbor, MI, USA, in 2014, where he is currently pursuing the Ph.D. degree.

His current research interests include fully integrated system clock generation, reference current generation, resistive sensor interface circuits, and wireless power transfer circuits for ultralow power

**Ziyun Li** (S'15) received the B.S. degree in electrical and computer engineering from the University of Michigan, Ann Arbor, MI, USA, in 2014, where he is currently pursuing the Ph.D. degree with the Michigan Integrated Circuit Laboratories.

His current research interests include high-performance, low power computer vision processing units to enable autonomous navigation of micro aerial vehicles.



**Zhihong Luo** was born in Shantou, China, in 1994. He is currently pursuing the B.S. degree at the University of Michigan, Ann Arbor, MI, USA, and Shanghai Jiaotong University, Shanghai, China.

His current research interests include embedded system design.



**Gyouho Kim** (M'09) received the B.S., M.S., and Ph.D. degrees in electrical engineering from the University of Michigan, Ann Arbor, MI, USA, in 2009, 2011, and 2014, respectively.

He is currently a Post-Doctoral Research Fellow with the University of Michigan. His current research interests include ultralow power very large scale integration design for energy-constrained system.



**Zhiyong Foo** received the B.S., M.S., and Ph.D. degrees in electrical engineering from the University of Michigan, Ann Arbor, MI, USA.

He is currently the Head of CubeWorks Inc., a startup spun out of the University of Michigan commercializing ultralow power systems. His current research interests include low cost and low power very large scale integration circuit systems integration.



**Hun-Seok Kim** (M'11) received the B.S. degree in electrical engineering from Seoul National University, Seoul, South Korea, and the M.S. and Ph.D. degrees in electrical engineering from the University of California at Los Angeles (UCLA), Los Angeles, CA, USA.

He was a Technical Staff Member with Texas Instruments Incorporated, Dallas, TX, USA, from 2010 to 2014, while serving as an Industry Liaison for multiple university projects funded by the Semiconductor Research Cooperation and Texas Instruments Incorporated. He is now an Assistant Professor with the University of Michigan, Ann Arbor, MI, USA. He currently holds nine granted patents and has over 10 pending applications in the areas of digital communication, signal processing, and low power integrated circuits. His current research interests include system novel algorithms and efficient very large scale integration architectures for low-power/high-performance signal processing, wireless communication, computer vision, and machine learning systems.

Dr. Kim was a recipient of multiple fellowships from the Ministry of Information and Telecommunication (South Korea), Seoul National University, and UCLA.



**David D. Wentzloff** (M'07) received the B.S.E. degree in electrical engineering from the University of Michigan, Ann Arbor, MI, USA, in 1999, and the M.S. and Ph.D. degrees from the Massachusetts Institute of Technology, Cambridge, MA, USA, in 2002 and 2007, respectively.

Since 2007, he has been with the University of Michigan, where he is currently an Associate Professor of Electrical Engineering and Computer Science. In 2012, he co-founded PsiKick, a fabless semiconductor company developing ultralow power wireless system on a chip. His current research interests include RF integrated circuits, with an emphasis on ultralow power design.

Prof. Wentzloff is a member of the IEEE Circuits and Systems Society, the IEEE Microwave Theory and Techniques Society, the IEEE Solid-State Circuits Society, and the Tau Beta Pi. He was a recipient of the 2009 DARPA Young Faculty Award from 2009 to 2010, the Eta Kappa Nu Professor of the Year Award, the 2011 DAC/ISSCC Student Design Contest Award, the 2012 IEEE Subthreshold Microelectronics Conference Best Paper Award, the 2012 NSF CAREER Award, the 2014 ISSCC Outstanding Forum Presenter Award, the 2014–2015 Eta Kappa Nu ECE Professor of the Year Award, the 2014–2015 EECS Outstanding Achievement Award, and the 2015 Joel and Ruth Spira Excellence in Teaching Award. He has served on the Technical Program Committee for ICUWB 2008–2010, ISLPED 2011–2015, S3S 2013–2014, and RFIC 2013–2015, and as a Guest Editor of the IEEE TRANSACTIONS ON MICROWAVE THEORY AND TECHNIQUES, the *IEEE Communications Magazine*, and the Elsevier journal *Signal Processing: Image Communication*.



**David Blaauw** (F'12) received the B.S. degree in physics and computer science from Duke University, Durham, NC, USA, in 1986, and the Ph.D. degree in computer science from the University of Illinois at Urbana–Champaign, Champaign, IL, USA, in 1991.

He was the Manager of the High Performance Design Technology group, Motorola, Inc., Austin, TX, USA. Since 2001, he has been with the faculty of the University of Michigan, Ann Arbor, MI, USA, where he is currently a Professor. He has authored over 500 papers and holds 50 patents. His current research interests include very large scale integration design with particular emphasis on ultralow power and high performance design for ultralow power sensor nodes.

Prof. Blaauw was the Technical Program Chair and the General Chair for the International Symposium on Low Power Electronic and Design. He was also the Technical Program Co-Chair of the ACM/IEEE Design Automation Conference and a member of the ISSCC Technical Program Committee.